PMU Algorithms Based on Adaptive Taylor–Fourier Models: A Three-Phase Compressive Sensing Method for Spectral Support Recovery

Guglielmo Frigo, *Senior Member, IEEE*, Paolo Attilio Pegoraro, *Senior Member, IEEE*, and Sergio Toscani, *Senior Member, IEEE*

***Abstract*— Phasor measurement units (PMUs) are the backbone of transmission grid monitoring and, in a likely future scenario, their use will be extended to distribution systems. This context stimulated the design of PMU algorithms that are more accurate and responsive, capable of tracking fast dynamics while rejecting the interference due to harmonics and interharmonics. An attractive approach relies on the identification of a Taylor–Fourier multifrequency (TFM) signal model that shall include all the significant narrowband components. In this respect, a proper detection of these components, representing the spectral support of the signal, has vital impact on accuracy. The present article improves the spectral support recovery technique adopted by the recently proposed compressive sensing weighted TFM (CS-WTFM) algorithm for synchrophasor, frequency, and rate of change of frequency (ROCOF) estimation. The underlying idea is considering the three-phase signal as a whole and leveraging its quasi three-phase symmetry. The developed measurement algorithm, called CS3-WTFM, searches for a shared spectral support among the three phases. It is analytically proven that, thanks to the aforementioned symmetry, it ensures a more robust and effective retrieval of the signal components with respect to a *per-phase* approach. Simulation results highlight that CS3-WTFM enables a remarkably higher accuracy in the presence of interharmonic interference. A dedicated selection of the window weights used in CS3-WTFM, leveraging the benefits of the three-phase support recovery, further improves performance.**

Received 26 November 2024; revised 11 February 2025; accepted 25 February 2025. Date of publication 19 March 2025; date of current version 3 April 2025. The work of Guglielmo Frigo was supported by the SFOE QUINPORTION Research Program under Grant SI/502415. The work of Paolo Attilio Pegoraro was supported by European Union—Next Generation EU, Mission 4, Component 2 through Italian Ministerial Grant PRIN 2022 "Smart Grid-Connected Power Converters Based on Advanced Synchrophasor-Inspired Harmonics Measurements for Holistic Integration Of Renewable Energy Sources (POWERHERO)", n° 20224X2AYH, CUP F53D23000490006. The work of Sergio Toscani was supported by European Union—Next Generation EU, Mission 4, Component 2 through Italian Ministerial Grant PRIN 2022 "Next-Generation Distributed Synchronized Measurement Systems for Smart Grids With Self-Diagnostics Capabilities and Self-Improvement of Information Quality" n° 2022RYZJT9, CUP D53D23001470006. The Associate Editor coordinating the review process was Dr. Ferdinanda Ponci. *(Corresponding author: Sergio Toscani.)*

Guglielmo Frigo is with the Electrical Energy and Power Laboratory, Swiss Federal Institute of Metrology, CH-3003 Bern-Wabern, Switzerland (e-mail: guglielmo.frigo@metas.ch).

Paolo Attilio Pegoraro is with the Department of Electrical and Electronic Engineering, University of Cagliari, 09123 Cagliari, Italy (e-mail: paolo.pegoraro@unica.it).

Sergio Toscani is with Dipartimento di Elettronica, Informazione e Bioingegneria, Politecnico di Milano, 20133 Milan, Italy (e-mail: sergio.toscani@polimi.it).

Digital Object Identifier 10.1109/TIM.2025.3552878

***Index Terms*— Compressive sensing (CS), frequency, phasor measurement unit (PMU), rate of change of frequency (ROCOF), symmetrical components, Taylor–Fourier multifrequency (TFM), three-phase waveforms.**

I. Introduction

TRADITIONALLY, transmission grids were monitored by means of supervisory control and data acquisition (SCADA) systems. The poor time resolution together with the unsynchronised nature of the measurements prevented an accurate reconstruction of the state, as well as capturing the time evolution during transients. In this regard, the availability of low-cost microprocessors and GPS technology enabled introducing phasor measurement units (PMUs) [1], thus overcoming the aforementioned limitations. For the first time, they made available accurate and frequent snapshots of phasors, frequency, and rate of change of frequency (ROCOF) in geographically remote nodes, timestamped according to a shared time coordinate.

Nowadays, PMUs are the backbone of wide area monitoring system (WAMS) for transmission grids; their measurements, thanks to the accurate timestamps referred to a shared timescale, are used for state estimation and for the detection of anomalous operating conditions, such as faults, oscillations, or incipient instability [2], and they are intended to be the input of the new wide area monitoring, protection, and control systems (WAMPACs) that are under design and implementation around the world to automate network management. The effectiveness of these applications strongly depends on different aspects, such as timeliness, latency [3], and above all on the accuracy of the provided measurements, affected by the metrological performance of the instrument transformers, but also by the adopted estimation algorithm [4], [5], [6], in particular as far as frequency and ROCOF are concerned. In this respect, standard IEC 60255-118-1:2018 [7] (IEC Std in what follows) defines two performance classes (P intended for low latency and fast response, M for high accuracy in slowly varying conditions) and the requirements that the PMU shall fulfill under different scenarios.

A large number of PMU algorithms can be found in the scientific literature, based on multifold approaches, including frequency tracking and tuned boxcar filters [8], least-square (LS) fitting of signal models [9], phase-locked loops [10], and Kalman filtering [11], [12]. Recently, efforts have been focused on enhancing the dynamic response, or on guaranteeing low latency and high accuracy in the presence of interharmonics or complex disturbances, considering more challenging conditions with respect to those prescribed by compliance tests. This research is also stimulated by the future installation of PMU-like devices in distribution networks [13], [14]. With respect to conventional PMUs, they are expected to face faster dynamics in the presence of stronger harmonics and interharmonics [15], [16].

Among all the algorithms, those based on Taylor–Fourier filters (TFFs) [17] are particularly interesting, thanks to their flexibility. They are suitable for tracking fast dynamics, as well as providing cancellation of disturbances coming from harmonics and interharmonics that could be included in the signal model, leading to the Taylor–Fourier multifrequency (TFM) approach [18]. Considering TFM-based methods, one may assume that interference is due to a sparse set of meaningful narrowband components, which can be identified by solving a compressive sensing (CS) problem, in turn enabling adaptive suppression of interferers. Performance highly depends on a proper retrieval of such components, representing the spectral support of the signal: neglected or poorly identified components may undermine the resulting filtering capability, thus degrading measurement accuracy. In this respect, the CS theory proves to be a valid solution, capable of improving spectral resolution without an unmanageable increase in computational complexity. However, the lack of a priori information regarding the number and location of the components makes the identification problem extremely prone to errors and misinterpretation.

It is worth noting that power systems are inherently three-phase and quasi balanced, thus meaning that the phase waveforms are very close to be periodic and identical, except for a time shift of one third of a period. For this very reason, a three-phase signal is not a mere juxtaposition of three *per-phase* components, but it should be considered as a whole. In fact, a three-phase signal is characterized by a single frequency (and ROCOF) value, as recommended by [7]. This peculiar feature leads to the formulation of inherently three-phase synchrophasor measurement methods [19], [20], [21], or to the evolution of algorithms originally intended to be individually applied to each phase signal [22], [23].

In [24], the CS-weighted TFM (CS-WTFM) approach [25] has been revisited to effectively cope with the three phases. A new CS-based three-phase spectral support recovery technique has been proposed, resulting in the CS3-WTFM method. When compared with the conventional, *per-phase* approach, it allows a more accurate detection of the narrowband components present in the analyzed signal, leading to a better TFM model capable of heavily mitigating their interference with fundamental-related estimates.

This article, which is the technical extension of [24], starts from a detailed analysis of the *per-phase* spectral support recovery adopted by CS-WTFM. Then, it presents a theoretical study showing how the three-phase support recovery technique exploits the quasi symmetry of power systems signals, resulting in inherently better performance. The analysis, carried out using symmetrical components, shows that the three-phase support recovery is less affected by spectral interference, thanks to the cancellation of some significant disturbing contributions that may undermine the *per-phase* approach.

The outcome of the study suggests that the advantages of the three-phase support recovery can be further enhanced through an ad hoc selection of the weighting window. In particular, its higher immunity to spectral interference enables exploiting, for a given two-cycle algorithm latency, the better frequency selectivity of a window having a narrower mainlobe, but higher sidelobes (i.e., leading to stronger spectral interference). Therefore, the weights for the CS3-WTFM method are generated from a properly tuned Kaiser window, leading to better overall accuracy with respect to that obtained with the usual Chebyshev window, typically adopted in conjunction with CS-WTFM.

The CS-WTFM (using the Chebyshev window) and CS3-WTFM (adopting both the Chebyshev and Kaiser windows) methods have been implemented and their performances have been compared in multifold scenarios, with test signals that simultaneously include multiple harmonics and an interharmonic, together with other off-nominal conditions. Achieved results clearly show the remarkable performance improvement enabled by CS3-WTFM, in particular when the tailored Kaiser window is adopted to generate the weights. Higher accuracy in synchrophasor, frequency, and ROCOF estimation is thus the outcome of the more robust three-phase spectral support recovery procedure.

II. CS-WTFM Approach

The CS-WTFM approach to synchrophasor, frequency, and ROCOF estimation relies on a TFM model for the analyzed segment of signal. As recalled in Section I, best performance occurs when the adopted TFM representation includes all the most significant spectral components actually present in the signal, so that it is possible to extract the fundamental component without infiltration of the others. In turn, such components are retrieved through an iterative procedure, based on the CS theory. The required steps of the technique are detailed in what follows.

A. TFM Models and PMU Estimates

Let us consider a three-phase power system having rated frequency f_0, thus corresponding to the angular frequency $\omega_0 = 2\pi f_0$. In this context, the class of TFM models provides an accurate parametric representation for voltage and current waveforms under typical operating conditions. Therefore, a vector $\mathbf{x}_p(t_r)$ (where $p \in \{a, b, c\}$), containing $N = 2L + 1$ samples[1] of the phase p signal $x_p(t)$ centered on the time instant $t = t_r$, can be expressed in the form

$$\mathbf{x}_p(t_r) = \begin{bmatrix} x_p(t_r + LT_s) \\ \vdots \\ x_p(t_r) \\ \vdots \\ x_p(t_r - LT_s) \end{bmatrix} = \bar{\mathbf{B}}_p \bar{\mathbf{p}}_p(t_r) + \mathbf{r}_p(t_r) \qquad (1)$$

[1] An odd number of samples is here adopted for the sake of presentation simplicity, without loss of generality.

where T_s is the sampling interval and overbars indicate complex-valued quantities. Vector $\mathbf{r}_p(t_r)$ represents the residual associated with t_r, containing the deviations between samples and their reconstructions from the model for a given parameters' vector $\bar{\mathbf{p}}_p(t_r)$, which in turn is

$$\bar{\mathbf{p}}_p(t_r) = \begin{bmatrix} \bar{X}_{p,1}^{(0)} & \cdots & \bar{X}_{p,1}^{(K_{p,1})} & \underline{X}_{p,1}^{(0)} & \cdots & \underline{X}_{p,1}^{(K_{p,1})} & \cdots & \underline{X}_{p,Q_p}^{(K_{p,Q_p})} \end{bmatrix}^{\mathsf{T}}. \quad (2)$$

Vector $\bar{\mathbf{p}}_p(t_r)$ thus includes the dynamic phasors $\bar{X}_{p,q}^{(0)}$ (with $q \in \{1, \ldots, Q_p\}$, each referred to the angular frequency $\omega_{p,q}$ and here expressed in root mean square, rms, magnitude) of all the considered components in the phase p signal, along with their successive derivatives $\bar{X}_{p,q}^{(k)}$ ($k \in \{1, \ldots, K_{p,q}\}$, being $K_{p,q}$ the adopted Taylor expansion degree) in $t = t_r$, which thus represents the measurement instant. In addition, the conjugates of these parameters (indicated through the underbar) must be included, since the waveform is inherently real-valued. Matrix $\bar{\mathbf{B}}_p$ is the model matrix (or measurement matrix) that can be written as

$$\bar{\mathbf{B}}_p = \begin{bmatrix} \bar{\mathbf{F}}(\omega_{p,1}, K_{p,1}) & \cdots & \bar{\mathbf{F}}(\omega_{p,Q_p}, K_{p,Q_p}) \end{bmatrix} \quad (3)$$

where $\bar{\mathbf{F}}(\omega, K)$ is given by

$$\bar{\mathbf{F}}(\omega, K) = \begin{bmatrix} \bar{\mathbf{\Phi}}(\omega) & \bar{\mathbf{\Phi}}^{\mathsf{H}}(\omega) \end{bmatrix} \mathbf{A}(K) \quad (4)$$

with $^{\mathsf{H}}$ denoting the Hermitian operator. Two types of matrices have to be introduced to fully define the structure of the signal model, i.e.,

$$\bar{\mathbf{\Phi}}(\omega) = \begin{bmatrix} e^{+j\omega L T_s} & & & & \\ & \ddots & & & \\ & & 1 & & \\ & & & \ddots & \\ & & & & e^{-j\omega L T_s} \end{bmatrix} \quad (5)$$

which is the phase-rotation matrix and

$$\mathbf{A}(K) = \frac{\sqrt{2}}{2} \begin{bmatrix} 1 & +LT_s & \frac{(+LT_s)^2}{2} & \cdots & \frac{(+LT_s)^K}{K!} \\ \vdots & \vdots & \vdots & & \vdots \\ 1 & 0 & 0 & & 0 \\ \vdots & \vdots & \vdots & & \vdots \\ 1 & -LT_s & \frac{(-LT_s)^2}{2} & \cdots & \frac{(-LT_s)^K}{K!} \end{bmatrix} \quad (6)$$

which is the Taylor time-lags matrix. The latter is the same for components sharing the Taylor expansion degree.

Considering power systems' waveforms, the first component having reference angular frequency $\omega_{p,1}$ always corresponds to the fundamental term, while the others can represent either harmonics or interharmonics. Let us assume that the set $\mathcal{S}_p = \{\omega_{p,q}\}_{q \in \{1,\ldots,Q_p\}}$, which is the spectral support of the TFM model, is somehow known in advance. Having selected proper expansion orders (capable of matching the expected dynamics of the components), the model matrix $\bar{\mathbf{B}}_p$ is fully defined, and an estimate of the model parameters in the measurement instant can be obtained as the solution of a weighted LS problem, i.e.,

$$\begin{aligned} \widehat{\bar{\mathbf{p}}}_p(t_r) &= \arg\min_{\bar{\mathbf{p}}} \left\| \mathbf{W}(\bar{\mathbf{B}}_p \bar{\mathbf{p}} - \mathbf{x}_p(t_r)) \right\|_2 \\ &= \arg\min_{\bar{\mathbf{p}}} \left\| \mathbf{r}_{w,p}(\bar{\mathbf{p}}, t_r) \right\|_2 \end{aligned} \quad (7)$$

with $\|\cdot\|_2$ indicating the Euclidean norm and $\widehat{\ }$ denoting estimates. Moreover

$$\mathbf{W} = \operatorname{diag}\left(\begin{bmatrix} w[+L] & \cdots & w[-L] \end{bmatrix}\right) \quad (8)$$

is the diagonal matrix of the weights, and $\mathbf{r}_{w,p}(\bar{\mathbf{p}}, t_r) = \mathbf{W}\mathbf{r}_p(\bar{\mathbf{p}}, t_r)$ is the weighted residual for a given parameter vector $\bar{\mathbf{p}}$. Therefore, according to (7), $\mathbf{x}_{w,p}(t_r) = \mathbf{W}\mathbf{x}_p(t_r)$ is approximated through a linear combination of the columns of $\bar{\mathbf{B}}_{w,p} = \mathbf{W}\bar{\mathbf{B}}_p$, namely, sampled rotating complex exponentials (their angular frequencies belong to $\mathcal{S}_p$) whose magnitudes vary proportionally to a power of the time distance with respect to the central entry, multiplied by the weights.

A proper choice of $\mathbf{W}$ enables increasing the sensitivity of the cost function to deviations occurring near the measurement instant. Hence, in the presence of misfit (that always occurs in practical applications), it helps improving the accuracy of the estimates. Assuming that $\bar{\mathbf{B}}_{w,p}$ has full column rank, the solution of (7) can be expressed as

$$\widehat{\bar{\mathbf{p}}}_p(t_r) = \bar{\mathbf{B}}_{w,p}^{\dagger} \mathbf{x}_{w,p}(t_r) = \bar{\mathbf{H}}_{w,p} \mathbf{x}_p(t_r) \quad (9)$$

where $\bar{\mathbf{B}}_{w,p}^{\dagger}$ is the Moore–Penrose inverse of $\bar{\mathbf{B}}_{w,p}$ while $\bar{\mathbf{H}}_{w,p} = \bar{\mathbf{B}}_{w,p}^{\dagger}\mathbf{W}$. Matrix $\bar{\mathbf{H}}_{w,p}$ defines a bank of FIR filters, called TFFs. Its mth row contains the complex-valued unit sample response of the TFF providing the estimate of $\bar{X}_{p,q}^{(l)}(t_r)$, i.e., the lth derivative of synchrophasor $\bar{X}_{p,q}^{(0)}(t_r)$ with $l = m - 1 - \sum_{i=1}^{q-1}(K_{p,q} + 1)$.

Having assumed $K_{p,1} \geq 2$, fundamental synchrophasor, frequency, and ROCOF estimates are obtained from the first three entries of $\widehat{\bar{\mathbf{p}}}_p(t_r)$, namely, $\widehat{\bar{X}}_{p,1}^{(k)}(t_r)$ with $k \in \{0, 1, 2\}$, as proven in [17]. Since a three-phase quantity is by definition characterized by unique frequency and ROCOF values, they are both obtained as average of the three *per-phase* estimates. All the quantities in this article are referred to the measurement instant but, for the sake of a lighter notation, the dependency on t_r will be omitted in the following.

B. CS-Based Support Recovery

As explained in Section II-A, defining the TFM model (1) requires retrieving the set of Q_p reference angular frequencies, which results in a set of estimates $\widehat{\omega}_{p,q}$. To achieve accurate measurements, the model should faithfully reflect the actual components in the signal, thus finding $\widehat{\omega}_{p,q} \approx \omega_{p,q}$ for each of them represents the preliminary stage. In this article, we rely on the CS theory and we adopt an iterative and greedy approach (as in [18]), i.e., we retrieve the spectral support as the set

$$\widehat{\mathcal{S}}_p = \{\nu_{p,i}, i \in \{1, \ldots, \widehat{Q}_p\}, \widehat{Q}_p \leq Q_{\max}\} \quad (10)$$

consisting of the angular frequencies $\nu_{p,i}$ belonging to the set

$$\mathcal{G} = \{h \cdot \delta_\omega, h \in \Gamma = \{1, \ldots, G\}\} = \delta_\omega \cdot \Gamma \quad (11)$$

with $G < \lfloor \pi/(T_s\delta_\omega) \rfloor$. According to (11), $\mathcal{G}$ represents a super-resolved frequency grid if $\delta_\omega < 2\pi/(NT_s)$. Each element of $\mathcal{G}$, indexed by h, corresponds to a column vector $\bar{\mathbf{d}}_h$ containing N samples of a complex exponential with angular frequency $h\delta_\omega$ and weighed by $\mathbf{W}$. The dictionary is defined as the set of all these column vectors (called atoms) that can be arranged in a matrix $\bar{\mathbf{D}}$; h thus indexes a column of $\bar{\mathbf{D}}$. $Q_{\max}$ is the assumed maximum number of components to seek, and the angular frequency $\nu_{p,i}$, retrieved during the ith iteration step, is found as

$$h_{p,i} = \arg\max_{h \in \Gamma_p^{[i-1]}} \left| \bar{\mathbf{d}}_h^{\mathsf{H}} \mathbf{r}_{w,p}^{[i-1]} \right| \tag{12}$$

$$\nu_{p,i} = h_{p,i} \cdot \delta_\omega \tag{13}$$

where $\mathbf{r}_{w,p}^{[i-1]}$ is the weighted residual obtained in the previous iteration (with $\mathbf{r}_{w,p}^{[0]} = \mathbf{x}_{w,p}$) while $\Gamma_p^{[i]} = \Gamma_p^{[i-1]} \backslash \{h_{p,i}\}$ (being $\Gamma_p^{[0]} = \Gamma$). Therefore, considering the generic ith iteration, the procedure consists of the following steps.

1) The starting points are the set $\Gamma_p^{[i-1]}$ of possible values for $h_{p,i}$, the weighted residual $\mathbf{r}_{w,p}^{[i-1]}$, and the model matrix $\widehat{\bar{\mathbf{B}}}_{w,p}^{[i-1]}$ ($\widehat{\bar{\mathbf{B}}}_{w,p}^{[0]}$ is an empty matrix), which have been either initialized or computed in the previous iteration.
2) $h_{p,i}$ is obtained according to (12) as the index of the atom resulting in the maximum absolute inner product with $\mathbf{r}_{w,p}^{[i-1]}$.
3) If the maximum magnitude of the inner product is below a threshold ρ_1, it means that the method has not detected a significant narrowband component, thus the support recovery process terminates. Otherwise, the angular frequency $\nu_{p,i} = h_{p,i}\delta_\omega$ is added to $\widehat{\mathcal{S}}_p$, then $\bar{\mathbf{F}}(\nu_{p,i}, J_{p,i})$ (with $J_{p,i}$ the chosen Taylor expansion degree for the component at hand) defined as in (4) is computed, multiplied by $\mathbf{W}$ and appended to $\widehat{\bar{\mathbf{B}}}_{w,p}^{[i-1]}$, thus obtaining $\widehat{\bar{\mathbf{B}}}_{w,p}^{[i]}$. Finally $\Gamma_p^{[i]}$ is prepared for the next iteration.
4) Vector $\widehat{\bar{\mathbf{p}}}_p$ is computed according to (9), but using $\widehat{\bar{\mathbf{B}}}_{w,p}^{[i]}$ instead of $\bar{\mathbf{B}}_{w,p}$. The corresponding weighted residual $\mathbf{r}_{w,p}^{[i]}$ is obtained, where the retrieved component should be heavily attenuated.
5) The procedure is iterated starting again from step 1, until the number of executions reaches $Q_{\max}$, or the Euclidean norm of the weighted residual falls under a predetermined threshold value η_1.

In the description above, Γ does not include $h = 0$ for the sake of simplicity, but also direct current can be dealt with by recalling that it does not involve an image component. Finally, it is worth highlighting that both the spectral support of the signal $\mathcal{S}_p$ and its estimate $\widehat{\mathcal{S}}_p$ are associated with the measurement instant and can thus change with time.

C. Investigating the Robustness of CS-Based Support Recovery

The final set $\widehat{\mathcal{S}}_p$ found with the CS procedure described in Section II-B includes the computed values $\nu_{p,i}$. Let us assume that the spectral support of phase p samples contains a component having reference angular frequency $\omega_{p,q}$. $\widehat{\mathcal{S}}_p$ should include an angular frequency $\nu_{p,i(q)}$ (where $i(q)$ is an appropriate index mapping) that represents the aforementioned $\widehat{\omega}_{p,q}$, i.e., the estimate of $\omega_{p,q}$. Ideally, the greedy procedure shall recover the optimal value $\tilde{\omega}_{p,q} = \tilde{h}_{p,q}\delta_\omega$ such that $|\tilde{\omega}_{p,q} - \omega_{p,q}| \le \delta_\omega/2$ due to grid resolution. However, this is not guaranteed: it occurs only if during an iteration (i.e., iteration $i(q)$), $\bar{\mathbf{d}}_{\tilde{h}_{p,q}}$ is the atom having the largest projection on the weighted residual $\mathbf{r}_{w,p}$ (the iteration index has been dropped for the sake of a lighter notation). Let us assume that $\mathbf{r}_{w,p}$ is a combination of sampled complex exponentials multiplied by $\mathbf{W}$. Therefore, its generic entry can be written in the form

$$r_{w,p}[n] \approx \frac{\sqrt{2}}{2} w[n] \sum_m \left(\bar{X}_{p,m} e^{j\omega_{p,m} n T_s} + \underline{X}_{p,m} e^{-j\omega_{p,m} n T_s} \right) \tag{14}$$

with $n \in \{-L, \ldots, L\}$. Under the assumption that the largely prevailing contribution comes from the exponential term having angular frequency $\omega_{p,q}$, the magnitude of the inner product between the residual and $\bar{\mathbf{d}}_{\tilde{h}_{p,q}}$ can be approximated as

$$u_{p,q} \approx \frac{\sqrt{2}}{2} \alpha_{p,q} |\bar{X}_{p,q}| \left(1 + \varepsilon_{p,q}\right) \tag{15}$$

having introduced the relative projection error as

$$\varepsilon_{p,q} \triangleq \Re \left\{ \bar{\gamma}_{p,q,q} e^{-j2\varphi_{p,q}} + \frac{1}{\bar{X}_{p,q}} \sum_{m \neq q} \left(\bar{\beta}_{p,q,m} \bar{X}_{p,m} + \bar{\gamma}_{p,q,m} \underline{X}_{p,m} \right) \right\} \tag{16}$$

with $\varphi_{p,q} = \angle \bar{X}_{p,q}$ and

$$\begin{aligned} \alpha_{p,q} &\triangleq |\bar{W}_2(j(\tilde{\omega}_{p,q} - \omega_{p,q}))| \\ \bar{\beta}_{p,q,m} &\triangleq \frac{\bar{W}_2(j(\tilde{\omega}_{p,q} - \omega_{p,m}))}{\bar{W}_2(j(\tilde{\omega}_{p,q} - \omega_{p,q}))} \\ \bar{\gamma}_{p,q,m} &\triangleq \frac{\bar{W}_2(j(\tilde{\omega}_{p,q} + \omega_{p,m}))}{\bar{W}_2(j(\tilde{\omega}_{p,q} - \omega_{p,q}))} \end{aligned} \tag{17}$$

being $\bar{W}_2(j\omega)$ the discrete-time Fourier transform (DTFT) of $w^2[n]$. Details are reported in Appendix A.

When looking at (15) and (16), $\varepsilon_{p,q} \neq 0$ occurs because the residual does not contain only the complex exponential having angular frequency $\omega_{p,q}$ but it includes other complex exponential terms, each one potentially having an impact on the magnitude of the inner product. In turn, according to (16), the relative projection error embeds two types of contributions. Those containing $\bar{\beta}_{p,q,m}$ come from the other complex exponential terms having positive angular speed. The contributions involving $\bar{\gamma}_{p,q,m}$ are produced by the negative frequency images, with $\bar{\gamma}_{p,q,q}$ associated with the image of the component to be retrieved. It is worth highlighting that according to the definitions in (17), the numerator of $\bar{\beta}_{p,q,m}$ and $\bar{\gamma}_{p,q,m}$ is the DTFT of the squared weights evaluated in the frequency separation between the optimal component within the dictionary and each interfering complex exponential present in the residual.

It is important to highlight that since $\varepsilon_{p,q} \neq 0$, it is possible that $u_{p,q}$ is not the largest projection, thus causing mistakes in spectral support recovery, with detrimental impact on the accuracy of synchrophasor, frequency, and ROCOF estimates. For a given dictionary coherence [26], quantifying the maximum similarity between atoms, the smallest the magnitude of $\varepsilon_{p,q}$, the highest the chance to retrieve the optimal frequency component $\tilde{\omega}_{p,q} \in \mathcal{G}$. Coherence decreases by refining the resolution δ_ω, but its value is also affected by the adopted weights [25]. Moreover, recalling (16) and (17), a proper selection of the weights that takes into account the expected spectral content of the signal may help reducing the projection error, thus improving the accuracy of the retrieved support.

III. Three-Phase Extension of the CS-WTFM Method

A. Three-Phase Approach to CS-Based Support Recovery

The CS approach described in Section II-B processes a vector $\mathbf{x}_p$ containing the N samples of phase p waveform, retrieving a spectral support $\widehat{\mathcal{S}}_p$. During the generic ith iteration, it identifies which vector $\bar{\mathbf{d}}_{h_{p,i}}$, among those belonging to the dictionary, captures the largest energy when it is projected on the weighted residual vector.

On the other hand, real-world power systems signals are close to be periodic and three-phase symmetric, hence the *per-phase* waveforms are very similar except for a time shift of one-third of the period. Moreover, a narrowband component at a given frequency is likely to appear on all the phases. This suggests that $\mathbf{x}_a$, $\mathbf{x}_b$, and $\mathbf{x}_c$ share the spectral support $\mathcal{S} = \{\omega_q\}_{q\in\{1,\dots,Q\}}$, thus they can be represented through TFM models whose structure is defined by the same matrix $\bar{\mathbf{B}} = \bar{\mathbf{B}}_a = \bar{\mathbf{B}}_b = \bar{\mathbf{B}}_c$.

To obtain an estimate $\widehat{\mathcal{S}}$ of the aforementioned spectral support, the CS procedure can be adapted to effectively leverage the three-phase nature of power systems' waveforms, thus looking at phases a, b, and c all together, resulting in the CS3-WTFM estimation method. For this reason, it is worth introducing the matrix of the three-phase samples

$$\mathbf{X} = \begin{bmatrix} \mathbf{x}_a & \mathbf{x}_b & \mathbf{x}_c \end{bmatrix} \tag{18}$$

together with its weighted counterpart $\mathbf{X}_w = \mathbf{W}\mathbf{X}$. During the ith iteration of the three-phase CS-based spectral recovery procedure, the previously obtained weighted three-phase residual, namely,

$$\mathbf{R}_w^{[i-1]} = \begin{bmatrix} \mathbf{r}_{w,a}^{[i-1]} & \mathbf{r}_{w,b}^{[i-1]} & \mathbf{r}_{w,c}^{[i-1]} \end{bmatrix} \tag{19}$$

is available. The intuitive underlying idea of the three-phase approach is seeking for the column of $\bar{\mathbf{D}}$, indexed by h_i, which is able to capture the highest overall energy from $\mathbf{R}_w^{[i-1]}$, thus

$$h_i = \underset{h\in\Gamma^{[i-1]}}{\arg\max} \left\| \bar{\mathbf{d}}_h^{\mathsf{H}} \mathbf{R}_w^{[i-1]} \right\|_2. \tag{20}$$

Similar to the *per-phase* approach, $\Gamma^{[0]} = \Gamma$, $\Gamma^{[i]} = \Gamma^{[i-1]} \backslash \{h_i\}$, and $\mathbf{R}_w^{[0]} = \mathbf{X}_w$. If the Euclidean norm of the largest three-phase projection is below the threshold ρ_3, the process stops, meaning that no significant narrowband components are detected. Otherwise, $\nu_i = h_i\delta_\omega$ is included in the retrieved support and the TFM model matrix (initialized as empty matrix) is updated as

$$\widehat{\bar{\mathbf{B}}}^{[i]} = \begin{bmatrix} \widehat{\bar{\mathbf{B}}}^{[i-1]} & \bar{\mathbf{F}}(\nu_i, J_i) \end{bmatrix} \tag{21}$$

where, similar to Section II-B, J_i is the Taylor expansion degree associated with the retrieved component. Introducing $\widehat{\bar{\mathbf{B}}}_w^{[i]} = \mathbf{W}\widehat{\bar{\mathbf{B}}}^{[i]}$, model parameters can then be obtained as

$$\widehat{\bar{\mathbf{P}}}_{abc}^{[i]} = \begin{bmatrix} \widehat{\bar{\mathbf{p}}}_a^{[i]} & \widehat{\bar{\mathbf{p}}}_b^{[i]} & \widehat{\bar{\mathbf{p}}}_c^{[i]} \end{bmatrix} = \left(\widehat{\bar{\mathbf{B}}}_w^{[i]} \right)^{\dagger} \mathbf{X}_w. \tag{22}$$

The process ends when the maximum number $Q_{\max}$ of iterations is reached, or when the Frobenius norm of the three-phase residual $\left\| \mathbf{R}_w^{[i]} \right\|_{\mathrm{F}}$ (namely, its total energy) drops below the threshold value η_3. The proposed three-phase support recovery technique is summarized in Algorithm 1. Having run such procedure, synchrophasors, frequency, and ROCOF estimates are obtained from $\widehat{\bar{\mathbf{p}}}_a$, $\widehat{\bar{\mathbf{p}}}_b$, and $\widehat{\bar{\mathbf{p}}}_c$, as explained at the end of Section II-A.

Algorithm 1 3ph CS-Based Support Recovery

Inputs: $\{\mathbf{x}_p\}_{p\in\{a,b,c\}}$
Parameters: $Q_{\max}$, $\{J_i\}_{i\in\{1,\dots,Q_{\max}\}}$, $\bar{\mathbf{D}}$, Γ, δ_ω, η_3, ρ_3
Outputs: $\widehat{\bar{\mathbf{p}}}_a$, $\widehat{\bar{\mathbf{p}}}_b$, $\widehat{\bar{\mathbf{p}}}_c$, $\widehat{\mathcal{S}}$

initialize $b_{\text{proj}} = 1$, $i = 1$, $\Gamma^{[0]} = \Gamma$, $\widehat{\mathcal{S}} = \emptyset$, $\widehat{\bar{\mathbf{B}}}_w^{[0]} = \emptyset$
initialize $\mathbf{X} = \begin{bmatrix} \mathbf{x}_a & \mathbf{x}_b & \mathbf{x}_c \end{bmatrix}$
initialize $\mathbf{X}_w = \mathbf{W}\mathbf{X} = \begin{bmatrix} \mathbf{x}_{w,a} & \mathbf{x}_{w,b} & \mathbf{x}_{w,c} \end{bmatrix}$
initialize residual $\mathbf{R}_w^{[0]} = \mathbf{X}_w$
compute overall energy of the residual $E_{\text{res}} = \left\| \mathbf{R}_w^{[0]} \right\|_{\mathrm{F}}$
while $E_{\text{res}} \geq \eta_3$ & $i \leq Q_{\max}$ & $b_{\text{proj}} == 1$ **do** - *support search*
  find the index $h_i = \arg\max_{h\in\Gamma^{[i-1]}} \left\| \bar{\mathbf{d}}_h^{\mathsf{H}} \mathbf{R}_w^{[i-1]} \right\|_2$
  and the corresponding projection energy E_{proj}
  if $E_{\text{proj}} \geq \rho_3$ **then**
    update $\widehat{\mathcal{S}} = \widehat{\mathcal{S}} \cup \{h_i\delta_\omega\}$
    update $\widehat{\bar{\mathbf{B}}}_w^{[i]} = \begin{bmatrix} \widehat{\bar{\mathbf{B}}}_w^{[i-1]} & \mathbf{W}\bar{\mathbf{F}}(h_i\delta_\omega, J_i) \end{bmatrix}$
    compute $\widehat{\bar{\mathbf{p}}}_p^{[i]} = \arg\min_{\bar{\mathbf{p}}} \left\| \mathbf{x}_{w,p} - \widehat{\bar{\mathbf{B}}}_w^{[i]} \bar{\mathbf{p}} \right\|_2$ for $p \in \{a, b, c\}$
    update $\mathbf{R}_w^{[i]} = \mathbf{X}_w - \widehat{\bar{\mathbf{B}}}_w \begin{bmatrix} \widehat{\bar{\mathbf{p}}}_a^{[i]} & \widehat{\bar{\mathbf{p}}}_b^{[i]} & \widehat{\bar{\mathbf{p}}}_c^{[i]} \end{bmatrix}$
    update $E_{\text{res}} = \left\| \mathbf{R}_w^{[i]} \right\|_{\mathrm{F}}$
    update $i = i + 1$
  else
    update $b_{\text{proj}} = 0$
  end
end
assign $\begin{bmatrix} \widehat{\bar{\mathbf{p}}}_a & \widehat{\bar{\mathbf{p}}}_b & \widehat{\bar{\mathbf{p}}}_c \end{bmatrix} = \begin{bmatrix} \widehat{\bar{\mathbf{p}}}_a^{[i-1]} & \widehat{\bar{\mathbf{p}}}_b^{[i-1]} & \widehat{\bar{\mathbf{p}}}_c^{[i-1]} \end{bmatrix}$
return

B. Comparing the Robustness of Per-Phase and Three-Phase CS-Based Support Recovery

After having introduced the three-phase CS-based support recovery, it is worth investigating its robustness following the same steps described in Section II-C for the single-phase case. We introduce the assumption that the sample vectors $\mathbf{x}_a$, $\mathbf{x}_b$, and $\mathbf{x}_c$ share the same underlying spectral support $\mathcal{S}$, as it happens in real-world situations. Therefore, in the generic ith iteration, let us assume that the three components of the weighted residual $\mathbf{R}_w$ are expressed by (14) with $p \in \{a, b, c\}$, while considering $\omega_{a,m} = \omega_{b,m} = \omega_{c,m} = \omega_m$. Supposing that the algorithm seeks for the angular frequency ω_q, ideally it should return the index $\tilde{h}_q$ corresponding to $\tilde{\omega}_q$, which differs from ω_q by at most half of the grid resolution. This occurs if $\bar{\mathbf{d}}_{\tilde{h}_q}$ is the atom $\bar{\mathbf{d}}_{h_i}$, resulting in the projection on the weighted three-phase residual whose Euclidean norm

$$u_q = \sqrt{u_{a,q}^2 + u_{b,q}^2 + u_{c,q}^2} \tag{23}$$

is the highest.

Supposing that each phase contribution $u_{a,q}$, $u_{b,q}$, and $u_{c,q}$ is mostly due to the component having angular frequency ω_q, their approximated expressions are given by (15), where $\alpha_{p,q}$, $\bar{\beta}_{p,q,m}$, and $\bar{\gamma}_{p,q,m}$ are replaced by α_q, $\bar{\beta}_{q,m}$, and $\bar{\gamma}_{q,m}$, defined analogously to (17) but involving the angular frequencies $\tilde{\omega}_q$, ω_q and ω_m shared by the three phases. After some passages, we obtain

$$u_q \approx \frac{\sqrt{2}}{2}\alpha_q X_{3\mathrm{ph},q}(1 + \varepsilon_q) \tag{24}$$

where

$$X_{3\mathrm{ph},q} = \left\| \begin{bmatrix} \bar{X}_{a,q} & \bar{X}_{b,q} & \bar{X}_{c,q} \end{bmatrix} \right\|_2 \tag{25}$$

is the three-phase rms value of the component having reference angular frequency ω_q and

$$\begin{aligned} \varepsilon_q = \frac{1}{X_{3\mathrm{ph},q}^2} \Re \Bigg\{ & \bar{\gamma}_{q,q} \left(\underline{X}_{a,q}^2 + \underline{X}_{b,q}^2 + \underline{X}_{c,q}^2 \right) \\ & + \sum_{m \neq q} \left[\bar{\beta}_{q,m} \left(\bar{X}_{a,m} \underline{X}_{a,q} + \bar{X}_{b,m} \underline{X}_{b,q} + \bar{X}_{c,m} \underline{X}_{c,q} \right) \right] \\ & + \sum_{m \neq q} \left[\bar{\gamma}_{q,m} \left(\underline{X}_{a,m} \underline{X}_{a,q} + \underline{X}_{b,m} \underline{X}_{b,q} + \underline{X}_{c,m} \underline{X}_{c,q} \right) \right] \Bigg\} \end{aligned} \tag{26}$$

represents the relative error of the three-phase projection. The three terms appearing in (26) are, respectively, due to the negative frequency image of the component associated with the angular frequency ω_q, to all the other complex exponentials contributions having positive angular speeds and to their respective negative frequency images. Similar to what happens in the *per-phase* approach, these contributions can make that the atom indexed by $\tilde{h}_q$ does not correspond to the largest norm of the three-phase projection, thus producing a suboptimal estimated support.

For a given dictionary, the robustness of support recovery is reflected by ε_q, which should be as small as possible. In this respect, it is worth performing a theoretical comparison between the three-phase and the *per-phase* support recovery. It is possible to demonstrate that using the same weights

$$|\varepsilon_q| \leq \max_{p \in \{a,b,c\}} |\varepsilon_{p,q}| \tag{27}$$

namely, that under the previous assumptions, the three-phase support recovery is at least as robust as the *per-phase* method (see Appendix B). Considering typical scenarios, three-phase systems are close to be symmetric. Therefore, it is interesting to evaluate the behavior of the three-phase relative projection error under this condition. For the purpose, phasors appearing in (26) are decomposed into their symmetrical components using the Fortescue transformation (computations are reported in Appendix C) thus obtaining

$$\begin{aligned} \varepsilon_q = \frac{1}{X_{3\mathrm{ph},q}^2} \Bigg[& \Re \left\{ \bar{\gamma}_{q,q} \left(2\underline{X}_{1,q}\underline{X}_{2,q} + \underline{X}_{0,q}^2 \right) \right\} \\ & + \sum_{m \neq q} \Re \left\{ \bar{\beta}_{q,m} \left(\bar{X}_{1,m}\underline{X}_{1,q} + \bar{X}_{2,m}\underline{X}_{2,q} + \bar{X}_{0,m}\underline{X}_{0,q} \right) \right\} \\ & + \sum_{m \neq q} \Re \left\{ \bar{\gamma}_{q,m} \left(\underline{X}_{1,m}\underline{X}_{2,q} + \underline{X}_{2,m}\underline{X}_{1,q} + \underline{X}_{0,m}\underline{X}_{0,q} \right) \right\} \Bigg] \end{aligned} \tag{28}$$

where, for each qth spectral component, $\bar{X}_{1,q}$, $\bar{X}_{2,q}$, and $\bar{X}_{0,q}$ are the phasors of the positive, negative, and zero sequence components, respectively. Three terms can be recognized in (28), having the same meaning as those appearing in (26), hence the below.

1) The first term is introduced by the negative frequency image of the spectral component to be retrieved in the three phases. It is due to the interaction between the positive and negative sequences, plus a term depending on the square of the zero sequence component. It is worth noting that this contribution to the projection error is maximized when either the spectral component to be retrieved is purely zero sequence or when its energy is equally split between positive and negative sequences. In those peculiar cases, considering (16), the contribution to the projection error due to the image equals that of the *per-phase* approach; otherwise, it is lower.
2) The second term is produced by the interaction of the spectral component to be retrieved in each phase with the other components present in the residual having positive angular frequencies. In this respect, interaction takes place exclusively between homologous symmetrical components.
3) The last term takes into account the interaction of the spectral component we are seeking in the three phases with the negative frequency images of all the other components, expressed as the sum of three addends. The positive sequence components interact exclusively with the images of the negative sequence components. Conversely, the negative sequence contribution of the component to be retrieved interacts only with the images of the other positive sequence components. Finally, the zero sequence contribution of the searched component just interferes with the images of the rest of the zero sequence components.

As highlighted in Section III-A, three-phase systems are very close to be symmetric during regular operation, with phase waveforms that are periodic and identical, except for a time shift corresponding to one-third of the period. This implies that the generic hth-order harmonic purely belongs to the sequence $s = h \bmod 3$ (mod is the modulo operation) with $s \in \{0, 1, 2\}$ corresponding to the zero, positive, and negative sequences, respectively.

Thanks to this property, the contribution to the three-phase projection error produced by the other interfering harmonics is induced by spectral components separated by at least three harmonic orders, thus corresponding to a frequency difference $\Delta\omega = 3\omega_1 \approx 3\omega_0$. Such a significant frequency separation makes that the effect of the interferers can be heavily mitigated, thanks to the coefficients $\bar{\beta}_{q,m}$ and $\bar{\gamma}_{q,m}$, proportional to $\bar{W}_2(j\Delta\omega)$, thus leveraging its low-pass behavior. A similar reasoning applies to the residual at each iteration of frequency support recovery.

It is important to highlight that the feature described in the previous paragraph represents a major advantage with respect to the *per-phase* support recovery, where all the harmonics contribute to the projection error (16). Moreover, because of the smaller frequency separation with the nearest interferers ($\Delta\omega = \omega_1 \approx \omega_0$), $\bar{\beta}_{p,q,m}$ and $\bar{\gamma}_{p,q,m}$ are much less effective in mitigating their impact, resulting in a higher chance of support recovery errors. Thus, the components' retrieval is improved with respect to the *per-phase* case, where, for each system phase, all the interferers, regardless of their symmetry, have an impact that depends on their magnitude and frequency distance. Errors in support recovery cannot even be compensated afterward through positive sequence synchrophasor extraction or by frequency and ROCOF averaging over the three *per-phase* estimates because the entire process is nonlinear and the three recovered spectral supports could be different. In addition, a significant reduction of computational cost is achieved by the shared support recovery, which leads to a unique TFM model definition, as it will be discussed in detail in Section III-C.

C. Analysis of Computational Load

From a computational viewpoint, CS3-WTFM and CS-WTFM share the same logical steps during every iteration of the algorithm. The first is identifying the best candidate component, followed by the second one, WTFM model estimation, which is influenced by the retrieved components.

Support recovery is performed iteratively ($Q_{\max}$ iterations at most), and thus the overall number of floating point operations (flops) depends on the spectral content of the analyzed three phase signal. Considering the three waveforms, the CS search algorithm involves, at the ith iteration, $3 \cdot |\Gamma^{[i-1]}| \cdot N$ multiplications for the inner products' computation to solve (12) for the three phases (CS-WTFM) or (20) (CS3-WTFM), other than $3N$ multiplications for residuals' weighting. Thus, the search is $\mathcal{O}(N)$, but it depends significantly on dictionary cardinality and atom size. In CS3-WTFM, Euclidean norm computation in (20) further takes three multiplications, which are indeed negligible. Then CS-WTFM requires obtaining the LS solution corresponding to (9) with the found measurement model matrix $\widehat{\bar{\mathbf{B}}}_{w,p}^{[i]}$ and $p \in \{a, b, c\}$ while CS3-WTFM relies on (22) and $\widehat{\bar{\mathbf{B}}}_{w}^{[i]}$. The main difference in terms of efficiency thus arises in these computations. CS-WTFM estimation requires obtaining three LS solutions associated with three different matrices (models are independently formulated for the three phases). The computational cost of the LS solution depends on the adopted algorithm. If the Householder QR decomposition is chosen, the size of $\widehat{\bar{\mathbf{B}}}_{w,p}^{[i]}$ ($N \times P_{p,i}$, with $P_{p,i} = \sum_{q=1}^{i}(2K_{p,q}+2)$ and $K_{p,q}$ the expansion degree of the qth component in phase p waveform) is relevant. If $P_{p,i} \ll N$ (which is always the case in the considered configurations), the main contribution in terms of flops is proportional to $P_{p,i}^2 N$, i.e., $\mathcal{O}(N)$. The solution is then obtained through an orthogonal matrix multiplication and backward substitution, which have a lower computational impact. CS3-WTFM instead requires performing a unique QR decomposition, thus this stage has almost one-third of the computational cost. Each iteration of both the methods is terminated by the residuals' energy computation.

It is also important to recall that the number of iterations of CS-WTFM can be different both among phases and with respect to CS3-WTFM, since it is based on three independent single-phase TFM models.

Finally, after iterations end, frequency and ROCOF computations rely on the estimated synchrophasor derivatives and take negligible time. Several optimizations could be adopted, but a full analysis of the computational burden in an ad hoc implementation is beyond the scope of this article.

IV. Methods' Configurations

The CS-WTFM and CS3-WTFM methods have been implemented to compare the obtained performance, considering $f_0 = 50$ Hz nominal frequency. They share most of the configuration parameters, including the sampling rate $f_s = 5$ kHz, the measurement reporting rate RR $= 50$ Hz, the data record length $N = 399$ (thus less than four nominal cycles, leading to an algorithm latency below 20 ms), the dictionary, and the Taylor expansion degrees. According to Section III-C, computational burden is heavily affected by the cardinality of the adopted frequency grid, hence by its resolution $\delta\omega$. Therefore, it must be chosen consistently with the available computational power. In this respect, $\delta_\omega = 2\pi$ rad/s has been selected, corresponding to 1 Hz frequency resolution. The fundamental component has been included in the TFM model through a second-order expansion (thus $K_1 = 2$), which is the least required by TF-based ROCOF estimation. Nonfundamental components have been considered through first-order expansions (namely, $K_q = 1$ for $q \neq 1$) that mitigate the impact of deviations between the actual reference frequencies of these components and the corresponding retrieved values.

The selection of the weights $w[n]$ affects overall performance in different ways. First, as discussed in Section II-A, it may improve the estimates in the presence of undermodeling (i.e., $\mathbf{x}_p$ does not belong to the subspace spanned by the columns of $\bar{\mathbf{B}}_p$); from a frequency domain point of view, it affects the pass bandwidths of the TFFs. However, the choice of the weights severely impacts the CS-based spectral support recovery of the TFM model. As shown in [25], $w[n]$

modifies the interatom coherence of the dictionary, since it reflects the magnitude of $\bar{W}_2(j\omega)$, with ω corresponding to the frequency separation between the considered atoms. Moreover, according to the findings presented in Sections II-C and III-B, the low-pass nature of $\bar{W}_2(j\omega)$ enables mitigating projection errors, thus improving the accuracy of the retrieved support.

In [24], the CS-WTFM and CS3-WTFM methods were compared adopting the same weights, obtained from the square root of a Chebyshev window having 45-dB sidelobe attenuation. This choice was originally proposed in [25] as a good tradeoff between frequency selectivity (or low dictionary coherence, associated with a narrow mainlobe) and low level of the first sidelobes, enabling better support recovery with respect to rectangular weighting.

Section III-B demonstrated that the three-phase projection error is sometimes equal, but typically lower than the *per-phase* case. Moreover, under symmetric conditions, it benefits from a three times wider frequency separation with the closest interferer. Therefore, when considering the selection of the weights, it is worth investigating the impact of moving the balance toward a sharper mainlobe (namely, lower dictionary coherence) sacrificing the attenuation of the first sidelobes. Adjusting the adopted Chebyshev window does not fit the purpose. In fact, during support recovery, the inner product between atom and residual could also be significantly affected by widely separated frequency components, as a consequence of the higher sidelobes combined with the equiripple behavior of the Chebyshev window [27].

The Kaiser window [28] approximates the digital prolate spheroidal sequence, which in turn maximizes the energy concentration in the mainlobe. The balance between the mainlobe width and sidelobe level is adjusted through the shape factor β_{Kaiser}; asymptotic sidelobe roll-off is the same as that of the rectangular window, namely, 20 dB/decade. These features make (the square root of) the Kaiser window particularly suitable for generating the weights to be adopted in the CS3-WTFM approach. In principle, the shape factor must be properly selected for the purpose, to optimize performance under a predetermined set of operating conditions, e.g., those described in Section V. However, it is extremely difficult to find out a systematic criterion, given the complexity of the problem. For this reason, the shape factor was varied with 0.1 step, and $\beta_{\text{Kaiser}} = 2$ resulted in a very favorable tradeoff between coherence and interference rejection.

Fig. 1 shows the DTFT magnitudes $|\bar{W}_2(j\omega)|$ for the considered Kaiser, Chebyshev, and rectangular windows. The DTFT of the selected Kaiser window features zeros close to frequencies multiples of f_s/N, thus also near 150 Hz, that is, when adopting the three-phase support recovery, the rated frequency separation between interfering components in the residual projection under ideal three-phase symmetry. When compared with the rectangular window, it features a slightly wider mainlobe, but significantly lower sidelobes. It is worth stressing that this Kaiser window does not enable improving overall performance when adopted in conjunction with *per-phase* support recovery, since it cannot rely on cancellations between projection error contributions from the different phases. As a consequence, the larger amplitude of the first sidelobes would result in significant projection errors, potentially causing mistakes in the retrieved spectral support, thus jeopardizing the benefits enabled by the narrower mainlobe.

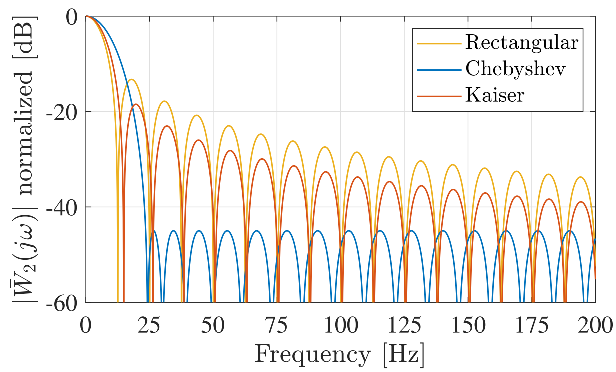

Fig. 1. DTFT magnitude of the rectangular, Chebyshev (−45 dB sidelobes), and Kaiser ($\beta_{\text{Kaiser}} = 2$) windows, $N = 399$.

To fully complete the configuration, the threshold values η_1 and ρ_1 of the CS-WTFM method have been, respectively, set to 10^{-3} and $2 \cdot 10^{-3}$ times the Euclidean norm of the weighted samples. As for the CS3-WTFM approach, η_3 and ρ_3 have been set to 10^{-3} and $2 \cdot 10^{-3}$ times the Frobenius norm of matrix $\mathbf{X}_w$, made of the weighted three-phase samples. Finally, $Q_{\max} = 6$ has been chosen as the maximum cardinality of the recovered spectral support.

V. Simulation Results

A. Base Test Signal

The comparison between CS-WTFM (with Chebyshev window) and CS3-WTFM (with Chebyshev or Kaiser windows) configured as described in Section IV has been carried out under static and dynamic scenarios going beyond IEC Std prescriptions, to stress the algorithms and explore their behaviors. All the test signals have been obtained by modifying or sweeping some parameters of a base waveform, whose characteristics are listed below.

1) The fundamental, positive sequence component has frequency $f_1 = 50.05$ Hz, so that it does not belong to the frequency grid $\mathcal{G}$ having 1-Hz resolution. This choice prevents the TFM model from fully embedding the fundamental, thus spectral support recovery becomes more demanding.
2) Three harmonics are always present, having orders 2, 3, and 5. Their amplitudes are 3%, 5%, and 4% of the fundamental, respectively. Three-phase symmetry is assumed (as in the harmonic distortion test prescribed by the IEC Std), hence the second- and fifth-order harmonics are negative sequence, while the third-order harmonic is a zero sequence contribution.
3) An interhamonic component having 10% magnitude and 12.2-Hz frequency is included, again not belonging to the super-resolved frequency grid, but located in the out-of-band region considering the adopted RR. The interharmonic is a positive sequence contribution, as in the out-of-band interference test of the IEC Std.

TABLE I

MAXIMUM ERRORS ACHIEVED BY THE CONSIDERED METHODS: DEFAULT CASE

Method	TVE_p [%]	TVE_1 [%]	|FE| [mHz]	|RFE| [Hz/s]
1ph, Cheb.	$6.5 \cdot 10^{-3}$	$2.3 \cdot 10^{-3}$	$6.9 \cdot 10^{-1}$	$3.6 \cdot 10^{-2}$
3ph, Cheb.	$4.0 \cdot 10^{-4}$	$2.2 \cdot 10^{-4}$	$3.4 \cdot 10^{-2}$	$3.7 \cdot 10^{-3}$
3ph, Kaiser	$7.3 \cdot 10^{-4}$	$2.2 \cdot 10^{-4}$	$8.9 \cdot 10^{-2}$	$1.1 \cdot 10^{-3}$

TABLE II

MAXIMUM ERRORS ACHIEVED BY THE CONSIDERED CS-BASED METHODS: DEFAULT CASE + UNBALANCE

Method	TVE_2 [%]	TVE_0 [%]	|FE| [mHz]	|RFE| [Hz/s]
1ph, Cheb.	$2.6 \cdot 10^{-1}$	$1.5 \cdot 10^{-1}$	$7.1 \cdot 10^{-1}$	$3.8 \cdot 10^{-2}$
3ph, Cheb.	$2.1 \cdot 10^{-2}$	$5.1 \cdot 10^{-3}$	$3.5 \cdot 10^{-2}$	$4.0 \cdot 10^{-3}$
3ph, Kaiser	$3.7 \cdot 10^{-2}$	$3.8 \cdot 10^{-3}$	$9.1 \cdot 10^{-2}$	$1.1 \cdot 10^{-3}$

Test duration has been set to 10 s, and while the considered methods have been configured for 50 Hz RR, estimates were provided with 100-Hz rate for the sake of a better statistical significance of the analysis. Performance is quantified in terms of total vector error (TVE), absolute frequency error (|FE|) and absolute ROCOF error (|RFE|).

B. Base Signal and Unbalance Test

First, the considered algorithms have been fed with the base test signal, featuring ideal three-phase symmetry except for the interharmonic component, which inherently breaks such symmetry. Achieved results are summarized in Table I in terms of maximum TVE for both *per-phase* (TVE_p, considering all the three phases) and positive sequence (TVE_1) synchrophasors, maximum |FE|, and maximum |RFE|.

In general, all the three implementations perform very well in this case. Three-phase support recovery enables lower errors (by roughly an order of magnitude) but anyway also those obtained with the *per-phase* approach can be considered negligible, except for the frequency estimate (maximum |FE| reaches 0.69 mHz). This is the result of repeated mistakes in locating the interharmonic component, which thus is not properly canceled and interferes with fundamental-related estimates. On the contrary, the three-phase approach (with both Chebyshev and Kaiser windows) always reaches the optimal support, leading to higher accuracy. TVEs are particularly low, as it occurs in most tests, hence their values will be often not reported. Positive sequence synchrophasor estimates benefit from the mutual cancellation of several error contributions (due to spectral interference) affecting *per-phase* estimates. It is worth mentioning that using the CS-WTFM method in conjunction with the Kaiser window results in a positive sequence TVE reaching 0.06%, |FE| is slightly lower than 4 mHz, while |RFE| exceeds 0.3 Hz/s. As somewhat expected from the considerations reported in Section IV, these values are substantially higher than those obtained with the same method but weights generated according to the Chebyshev window.

Real-world operating conditions may include (weak) imbalance. To explore accuracy in this scenario, the base test signal has been modified by including 2% unbalance at the fundamental (equally subdivided between negative and zero sequences) and 10% unbalance at each included harmonic (as before, evenly shared between the two symmetrical components breaking three-phase symmetry). Errors are shown in Table II, including the TVE values for the negative (TVE_2) and zero sequence synchrophasors (TVE_0). *Per-phase* and positive sequence TVEs are omitted, being negligible and virtually identical to those already reported in Table I.

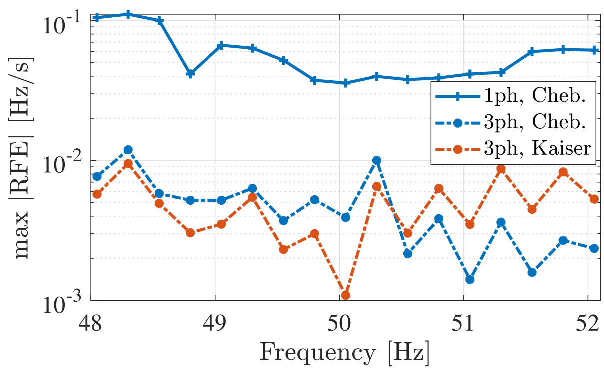

Fig. 2. Maximum |RFE| achieved by the considered CS-based methods: default case + off-nominal frequency.

Errors in frequency and ROCOF estimations are almost the same as those obtained under symmetric conditions. This confirms the better performance enabled by three-phase support recovery (similar results with both the considered weightings), in particular as far as frequency estimation is concerned, while exhibiting robustness with respect to fundamental and harmonic unbalance. Moreover, the *per-phase* support recovery and the resulting worse cancellation of the interference due to the interharmonic produce notable errors in negative and zero sequence synchrophasor estimates (maximum TVEs are 0.26% and 0.15%, respectively). On the contrary, the three-phase methods return excellent measurements.

C. Off-Nominal Frequency Test

The estimation errors of the implemented methods have been evaluated by considering the base signal, but varying the fundamental frequency from 48.05 to 52.05 Hz with 0.25-Hz step. Fig. 2 reports the obtained maximum |RFE| values.

Using the Chebyshev or Kaiser window, CS3-WTFM largely outperforms CS-WTFM since, over the whole fundamental frequency range, the former always retrieves the best spectral support, given the adopted 1-Hz grid step. A better modeling of harmonics and interharmonic results in a stronger cancellation of their impact on fundamental-related estimates (indeed, zeros in the FIR filter are finely tuned to suppress the detected interferences). Maximum |RFE| is thus reduced from above 0.1 Hz/s, using the *per-phase* support recovery, to about one order of magnitude lower. Similar considerations can be drawn from |FE| values, while synchrophasor estimates are excellent also when adopting the CS-WTFM method, since they are notably less sensitive to spectral interference. Dictionary granularity is responsible for the jagged error trends of the two CS3-WTFM implementations. This behavior is not

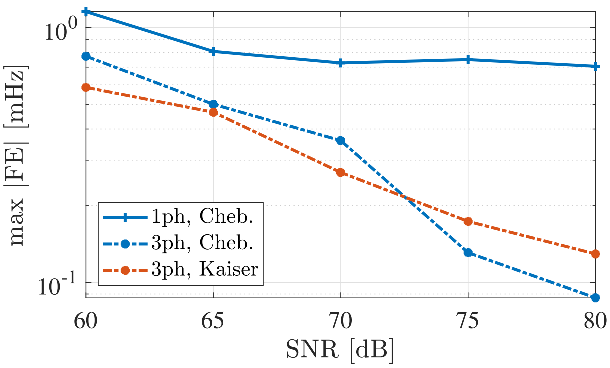

Fig. 3. Maximum |FE| achieved by the considered CS-based methods: default case + additive noise.

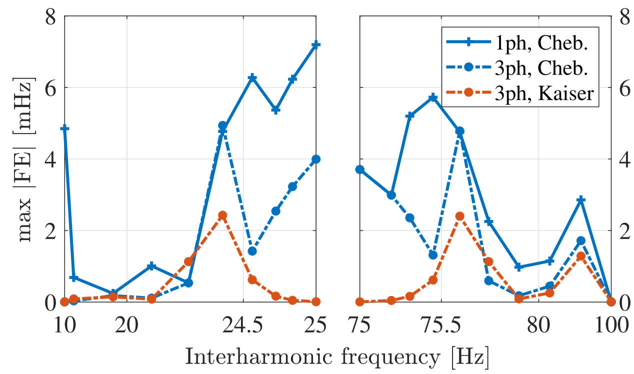

Fig. 4. Maximum |FE| achieved by the considered CS-based methods: default case + frequency sweep of the positive sequence interharmonic.

visible from the errors of CS-WTFM, since it is masked by a much stronger infiltration of the interharmonic.

D. Noise Sensitivity Test

In this article results are obtained without any wideband noise, to make more evident the differences between the considered implementations. However, it is worth investigating their robustness when white uniform noise at different signal-to-noise ratios (SNRs) is added to the default case. Fig. 3 depicts the maximum |FE| values, with SNR ranging from 60 to 80 dB.

CS-WTFM reaches 1.2 mHz |FE| at the lowest SNR level, while settling around 0.7 mHz as SNR is better than 70 dB. Here, the impact of noise becomes weak with respect to error contributions due to the other disturbances (in particular the interharmonic) that set a bound for accuracy.

In contrast, the two CS3-WTFM implementations exhibit a virtually linear decrease of the errors with the SNR level (in a log–log scale) thus highlighting the proportionality between noise standard deviation and |FE|. This reveals that results are still dominated by noise even at 80 dB SNR. As far as maximum |RFE| is concerned, which is notably even more sensitive with respect to wideband noise (since it depends on a second-order derivative), the same behavior is observed.

E. Interharmonic Frequency Sweep Tests

As discussed in Section III-B, the three-phase spectral support recovery is more robust, thanks to the cancellation of several interfering contributions in the inner products between atoms and residual. In particular, under the introduced assumptions, (28) shows that the projection error in retrieving a positive (negative) sequence component is solely due to the other positive frequency, positive (negative) sequence components, or negative frequency images of negative (positive) sequence component. Moreover, the projection error in seeking a zero sequence component is exclusively affected by all the other zero sequence contributions present in the three-phase residual. Benefits are already evident from the previous results, but it is worth better analyzing the behavior of the algorithms by sweeping the interharmonic frequency of the default case from 10 to 25 Hz, and from 75 to 100 Hz, considering the values suggested by [7].

Fig. 4 reports the results in terms of |FE|, showing the remarkable performance improvement enabled by the three-phase support recovery. As from Section III-B, for given conditions the three-phase approach always enables better or, in very specific cases, equal robustness. The *per-phase* approach heavily suffers from mistakes in retrieving the 10 Hz interharmonic (maximum |FE| $\approx$ 4.8 mHz) due to the projection errors induced by its negative frequency image. As explained in the previous paragraph, this does not occur as far as a three-phase approach is adopted, resulting in negligible |FE|.

When considering interharmonic frequency values approaching 25 or 75 Hz, both the three-phase and *per-phase* support recovery may suffer from interference between fundamental and interharmonic (both positive sequence). This is evident from Fig. 4, with CS-WTFM exceeding 7 mHz |FE|, but also CS3-WTFM with Chebyshev weighting reaching 4 mHz. Instead, CS3-WTFM adopting weights obtained from the Kaiser window results in virtually zero frequency error, thanks to the narrower mainlobe. This implementation reaches the best performance in this test, with an overall maximum |FE| of 2.4 mHz, less than half of that achieved when the Chebyshev window is adopted (4.9 mHz). Similar conclusions can be drawn when looking at the |RFE| values, not reported in detail for the sake of brevity. In this case, CS-WTFM achieves a rather high overall maximum |RFE| exceeding 1.1 Hz/s; CS3-WTFM enables reducing it to 0.7 Hz/s with the Chebyshev window and to 0.34 Hz/s, thanks to the Kaiser window.

The same interharmonic frequency sweep analysis has been carried out again, now considering a negative sequence interharmonic; Fig. 5 reports the maximum |RFE| values. In general, this condition is less demanding with respect to the previous case, as notable from the lower error values. Considering the conventional CS-WTFM method, maximum |RFE| is high for 10-Hz interharmonic frequency, as well as when the interferer approaches 25 Hz (reaching about 0.6 Hz/s) similar to what happened in case of a positive sequence interharmonic. The key difference occurs for the CS3-WTFM method, providing low errors even when the Chebyshev window is adopted and the interharmonic frequency is close to 25 or 75 Hz. This happens since the

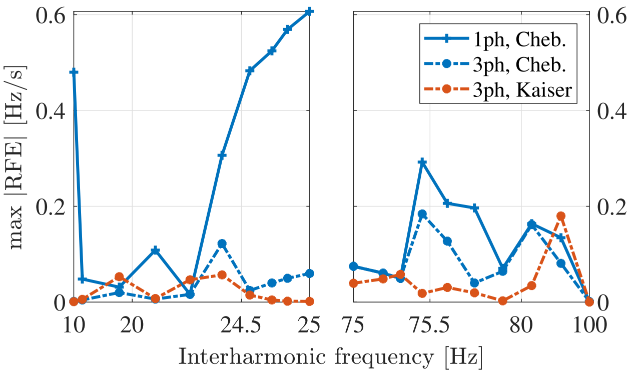

Fig. 5. Maximum |RFE| achieved by the considered CS-based methods: default case modified with negative sequence interharmonic (frequency sweep).

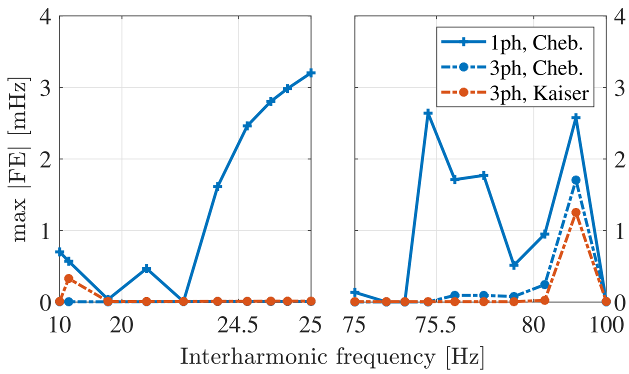

Fig. 6. Maximum |FE| achieved by the considered CS-based methods: default case modified with zero sequence interharmonic (frequency sweep).

interharmonic belongs to a different sequence with respect to the fundamental, thus the latter weakly affects the projection errors when searching the former, thanks to the three-phase support recovery. Anyway, the CS3-WTFM method with the Kaiser window results in slightly better overall accuracy.

The analysis has been repeated now considering a zero sequence interharmonic. It is worth noting that for low interharmonic frequencies, the CS3-WTFM method does not always recover the optimal support. The reason is the spectral interference between the zero sequence interharmonic and its negative frequency image during the support recovery stage, which cannot be mitigated by the three-phase approach (see (28)). As a consequence, in this frequency region the *per-phase* TVEs obtained with CS-WTFM and CS3-WTFM techniques adopting the same Chebyshev window are very close. The CS3-WTFM performs better when combined with the Kaiser window, thanks to its narrower mainlobe. The advantages of the three-phase support recovery become evident when looking at frequency and ROCOF estimates. The consistent spectral support among the three phases results in identical TFFs. This makes that the disturbances in *per-phase* frequency and ROCOF estimates due to the infiltration of zero sequence components can be heavily mitigated, thanks to the averaging process [29].

The maximum |FE| values are summarized in Fig. 6. It is evident how CS3-WTFM results in negligible errors, except when the interharmonic frequency is very close to that of the second-order harmonic. In that case, frequency separation is below half width of the mainlobe for all the adopted windows; the unavoidable spectral interference makes that the second-order harmonic is not properly located and canceled. The same conclusion can be drawn when analyzing the results in terms of maximum |RFE|.

According to (28), the projection error due to the negative frequency image of the component to be retrieved is maximum also when its energy is equally split into positive and negative sequences. Hence, the interharmonic frequency sweep has been carried out under this condition too. The maximum |RFE| values achieved by the analyzed methods are shown in Fig. 7. Considering a low-frequency interharmonic, errors in its location during spectral support recovery are dominated by interference with its negative frequency image, in this case

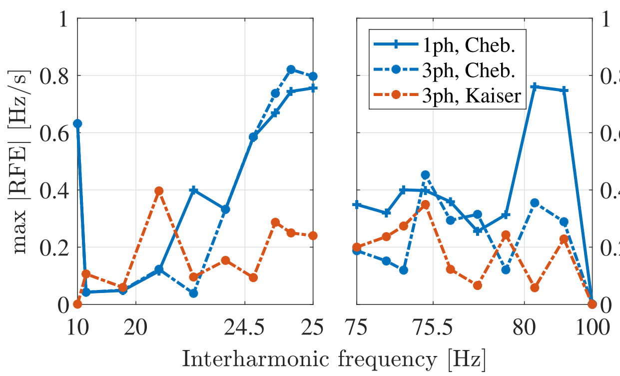

Fig. 7. Maximum |RFE| achieved by the considered CS-based methods: default case modified with positive + negative sequence interharmonic (frequency sweep).

identical for both the *per-phase* and three-phase approaches. In fact, adopting the same Chebyshev window, CS-WTFM and CS3-WTFM achieve almost the same performance in this case. However, accuracy attained by the CS3-WTFM method can be significantly improved, thanks to the Kaiser window, exploiting its narrower mainlobe.

F. Amplitude and Phase Modulation Tests

One of the advantages of the Taylor–Fourier model-based approaches is that they can include signal dynamics, leading to good accuracy under these conditions. In this regard, the performances of the three implementations have been evaluated as the fundamental of the base signal undergoes sinusoidal amplitude modulation (AM) or when both the fundamental and harmonics are subject to sinusoidal phase modulation (PM) (see [7] for waveform equations). Modulation depth is 10% in AM, 0.1 rad in PM, while modulation frequency is varied up to 2 Hz. Errors are summarized in Tables III and IV for AM and PM, respectively; Fig. 8 reports instead the trend of maximum |FE| obtained by varying the modulation frequency in the AM case.

When considering AM, the three methods achieve rather small errors, but once again the three-phase support recovery enables the best accuracy. As notable from Fig. 8, the performance of CS-WTFM is barely affected by the modulation frequency, since the mistakes in the retrieved support mask

TABLE III
MAXIMUM ERRORS ACHIEVED BY THE CONSIDERED METHODS: DEFAULT CASE + AMPLITUDE MODULATION

Method	TVE_p [%]	TVE_1 [%]	|FE| [mHz]	|RFE| [Hz/s]
1ph, Cheb.	$8.5 \cdot 10^{-3}$	$3.6 \cdot 10^{-3}$	1.0	$4.0 \cdot 10^{-2}$
3ph, Cheb.	$2.1 \cdot 10^{-3}$	$1.5 \cdot 10^{-3}$	0.32	$6.4 \cdot 10^{-3}$
3ph, Kaiser	$4.3 \cdot 10^{-3}$	$1.6 \cdot 10^{-3}$	0.45	$1.4 \cdot 10^{-2}$

TABLE IV
MAXIMUM ERRORS ACHIEVED BY THE CONSIDERED METHODS: DEFAULT CASE + PHASE MODULATION

Method	TVE_p [%]	TVE_1 [%]	|FE| [mHz]	|RFE| [Hz/s]
1ph, Cheb.	$1.1 \cdot 10^{-2}$	$6.4 \cdot 10^{-3}$	4.2	$1.2 \cdot 10^{-1}$
3ph, Cheb.	$8.4 \cdot 10^{-3}$	$4.4 \cdot 10^{-3}$	3.6	$8.9 \cdot 10^{-2}$
3ph, Kaiser	$7.9 \cdot 10^{-3}$	$4.3 \cdot 10^{-3}$	4.5	$7.0 \cdot 10^{-2}$

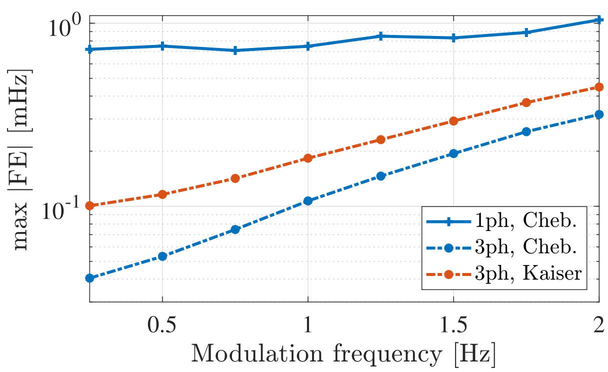

Fig. 8. Maximum |FE| achieved by the considered CS-based methods: AM frequency sweep.

error contributions due to the dynamics. Conversely, the accuracy of CS3-WTFM implementations (that always retrieve the optimal support) is sensitive to the modulation frequency. The Chebyshev window leads to slightly better performance, since it results in a slightly larger bandwidth of the TFFs, which thus enables a better tracking of the time-varying fundamental.

PM represents a more demanding scenario for the algorithms, leading to significant error contributions due to the dynamics. This attenuates the impact of interharmonics interference that occurs when it is not optimally embedded in the spectral support of the TFM model. As a result, considering the highest 2 Hz modulation frequency, CS3-WTFM performs slightly better than CS-WTFM.

To check the feasibility of a real-time implementation of the proposed method, average execution times have been recorded considering the MATLAB scripts used for the tests, running in a PC equipped with Intel-Core[2] i9-11900 CPU at 2.50 GHz. As a first comment, it is essential to stress that no specific parallelization or optimization of the code was adopted, since the aim was to get a preliminary idea about feasibility. Even if a real-time implementation is beyond the scope of the present article and computational burden depends on the signal composition, the constraint was easily met for both the methods even with RR = 100 Hz, since execution time was below 5 ms in all the tests. Moreover, thanks to the speed up provided by CS3-WTFM and discussed in Section III-C, it runs at least 20% faster than CS-WTFM.

VI. CONCLUSION

This article proposes the CS3-WTFM method for synchrophasor, frequency, and ROCOF estimation as an improved version of the CS-WTFM algorithm. The main difference consists in the spectral support recovery of the TFM model, which leverages the inherent three-phase nature of power systems signals. In this respect, CS3-WTFM seeks a unique spectral support shared by the three phases, through an iterative greedy algorithm that jointly processes the three-phase samples. It has been theoretically proven why, thanks to the quasi symmetry of power system waveforms, the three-phase support recovery is much more efficient and accurate than the *per-phase* approach that the CS-WTFM method is based on.

The selection of the weights has a dramatic impact on overall performance. Theoretical considerations suggest that the CS3-WTFM method could benefit by a different weighting, based on the Kaiser window, with respect to that commonly adopted in CS-WTFM implementations (based on the Chebyshev window) trading the mitigation of spectral interference for a finer frequency selectivity. This aspect will be further investigated in the future steps of this research, looking for an adaptive tradeoff between rejection of spurious components and low dictionary coherence during spectral support recovery.

The CS-WTFM and CS3-WTFM methods have been compared under a wide range of conditions. The results clearly show the remarkable performance improvement (particularly as far as frequency and ROCOF estimates are concerned) enabled by the three-phase support recovery approach, with the best results achieved when weights are obtained from a tailored Kaiser window. The main benefit comes from the more accurate location of interharmonics, so that the interference with fundamental-related estimates can be effectively suppressed by the resulting TFFs. This feature is extremely important in modern power systems, which are more and more frequently affected by sub- and interharmonic disturbances, and it can foster the application of the algorithm in PMUs for both transmission and distribution systems. Furthermore, it opens the door to further developments in the context of real-time harmonic and interharmonic synchronized measurements.

APPENDIX A
OBTAINING THE MAGNITUDE OF THE INNER PRODUCT BETWEEN OPTIMAL ATOM AND RESIDUAL

Starting from (14), reminding the definition of $\bar{\mathbf{d}}_{\tilde{h}_{p,q}}$ while performing some manipulations it is possible to obtain

$$\begin{aligned} u_{p,q} &= |\bar{\mathbf{d}}^{\mathsf{H}}_{\tilde{h}_{p,q}} \mathbf{r}_{w,p}| \\ &= \frac{\sqrt{2}}{2} \left| \sum_m \left(\bar{X}_{p,m} \sum_{n=-L}^{L} w^2[n] e^{-j(\tilde{\omega}_{p,q}-\omega_{p,m})nT_s} \right.\right. \\ &\qquad \left.\left. + \underline{X}_{p,m} \sum_{n=-L}^{L} w^2[n] e^{-j(\tilde{\omega}_{p,q}+\omega_{p,m})nT_s} \right) \right| \end{aligned} \quad (29)$$

[2]Trademarked.

that, recognizing the DTFT of $w^2[n]$ and using the definitions (17), can be rewritten as

$$u_{p,q} = \frac{\sqrt{2}}{2}\alpha_{p,q}|\bar{X}_{p,q}|\sqrt{\left(1+\Re\left\{\bar{\mu}_{p,q}\right\}\right)^2 + \left(\Im\left\{\bar{\mu}_{p,q}\right\}\right)^2} \tag{30}$$

having introduced

$$\bar{\mu}_{p,q} = \bar{\gamma}_{p,q,q}e^{-j2\varphi_{p,q}} + \frac{1}{\bar{X}_{p,q}}\sum_{m\neq q}\left(\bar{\beta}_{p,q,m}\bar{X}_{p,m} + \bar{\gamma}_{p,q,m}\underline{X}_{p,m}\right). \tag{31}$$

Assuming that the largely prevailing contribution to $u_{p,q}$ is produced by the component to be recovered, $|\bar{\mu}_{p,q}| \ll 1$, hence (30) can be well-approximated as

$$\begin{aligned} u_{p,q} &\approx \frac{\sqrt{2}}{2}\alpha_{p,q}|\bar{X}_{p,q}|\sqrt{1+2\Re\left\{\bar{\mu}_{p,q}\right\}} \\ &\approx \frac{\sqrt{2}}{2}\alpha_{p,q}|\bar{X}_{p,q}|\left(1+\Re\left\{\bar{\mu}_{p,q}\right\}\right). \end{aligned} \tag{32}$$

Finally, (15) is obtained by defining $\varepsilon_{p,q} = \Re\{\bar{\mu}_{p,q}\}$.

Appendix B
Comparing Per-Phase and Three-Phase Relative Projection Errors

Rearranging (26) and reminding (16), the magnitude of the three-phase relative projection error can be written as

$$|\varepsilon_q| = \frac{1}{X^2_{3\text{ph},q}}\left||\bar{X}_{a,q}|^2\varepsilon_{a,q} + |\bar{X}_{b,q}|^2\varepsilon_{b,q} + |\bar{X}_{c,q}|^2\varepsilon_{c,q}\right|. \tag{33}$$

Thanks to the generalized triangle inequality

$$|\varepsilon_q| \leq \frac{1}{X^2_{3\text{ph},q}}\left(|\bar{X}_{a,q}|^2|\varepsilon_{a,q}| + |\bar{X}_{b,q}|^2|\varepsilon_{b,q}| + |\bar{X}_{c,q}|^2|\varepsilon_{c,q}|\right). \tag{34}$$

Finally, reminding the definition of the three-phase rms value, (27) is obtained.

Appendix C
Expressing the Three-Phase Relative Projection Error in Terms of Symmetrical Components

Considering the generic qth spectral component, let us define the column vector of the three-phase phasors as

$$\bar{\mathbf{p}}_{abc,q} = \left[\bar{X}_{a,q} \quad \bar{X}_{b,q} \quad \bar{X}_{c,q}\right]^{\mathsf{T}} \tag{35}$$

so that, substituting in (26), ε_q can be written as

$$\varepsilon_q = \frac{1}{X^2_{3\text{ph},q}}\Re\left\{\bar{\gamma}_{q,q}\bar{\mathbf{p}}^{\mathsf{H}}_{abc,q}\underline{\mathbf{p}}_{abc,q} + \sum_{m\neq q}\left(\bar{\beta}_{q,m}\bar{\mathbf{p}}^{\mathsf{H}}_{abc,q}\bar{\mathbf{p}}_{abc,m} + \bar{\gamma}_{q,m}\bar{\mathbf{p}}^{\mathsf{H}}_{abc,q}\underline{\mathbf{p}}_{abc,m}\right)\right\}. \tag{36}$$

Introducing $\bar{\mathbf{T}}$ as the Fortescue transformation matrix (the unitary formulation is adopted), we have

$$\bar{\mathbf{p}}_{012,q} = \bar{\mathbf{T}}\bar{\mathbf{p}}_{abc,q}, \quad \bar{\mathbf{T}}^{-1} = \bar{\mathbf{T}}^{\mathsf{H}} \tag{37}$$

with

$$\bar{\mathbf{p}}_{012,q} = \left[\bar{X}_{0,q} \quad \bar{X}_{1,q} \quad \bar{X}_{2,q}\right]^{\mathsf{T}}. \tag{38}$$

Using (37) into (36) leads to

$$\varepsilon_q = \frac{1}{X^2_{3\text{ph},q}}\Re\left\{\bar{\gamma}_{q,q}\underline{\mathbf{p}}^{\mathsf{T}}_{012,q}\bar{\mathbf{T}}\bar{\mathbf{T}}^{\mathsf{T}}\underline{\mathbf{p}}_{012,q} + \sum_{m\neq q}\left(\bar{\beta}_{q,m}\underline{\mathbf{p}}^{\mathsf{T}}_{012,q}\bar{\mathbf{p}}_{012,m} + \bar{\gamma}_{q,m}\underline{\mathbf{p}}^{\mathsf{T}}_{012,q}\bar{\mathbf{T}}\bar{\mathbf{T}}^{\mathsf{T}}\underline{\mathbf{p}}_{012,m}\right)\right\} \tag{39}$$

that, after few simple manipulations, results in (28).

References

[1] A. G. Phadke, J. S. Thorp, and M. G. Adamiak, "A new measurement technique for tracking voltage phasors, local system frequency, and rate of change of frequency," *IEEE Power Eng. Rev.*, vol. PER-3, no. 5, pp. 1025–1038, May 1983.

[2] J. De La Ree, V. Centeno, J. S. Thorp, and A. G. Phadke, "Synchronized phasor measurement applications in power systems," *IEEE Trans. Smart Grid*, vol. 1, no. 1, pp. 20–27, Jun. 2010.

[3] P. Castello, G. Gallus, P. A. Pegoraro, and S. Sulis, "Measurement platform for latency characterization of wide area monitoring, protection and control systems," *IEEE Trans. Instrum. Meas.*, vol. 73, pp. 1–12, 2024.

[4] I. Kamwa, S. R. Samantaray, and G. Joos, "Compliance analysis of PMU algorithms and devices for wide-area stabilizing control of large power systems," *IEEE Trans. Power Syst.*, vol. 28, no. 2, pp. 1766–1778, May 2013.

[5] Working Group C4.34—Power System Technical Performance, "Application of phasor measurement units for monitoring power system dynamic performance," CIGRE, Paris, France, Tech. Brochure 702, Sep. 2017.

[6] G. Frigo, A. Derviškadić, Y. Zuo, and M. Paolone, "PMU-based ROCOF measurements: Uncertainty limits and metrological significance in power system applications," *IEEE Trans. Instrum. Meas.*, vol. 68, no. 10, pp. 3810–3822, Oct. 2019.

[7] *IEEE/IEC International Standard-measuring Relays and Protection Equipment—Part 118-1: Synchrophasor for Power System-Measurements*, document IEC/IEEE 60255-118-1:2018, 2018.

[8] A. J. Roscoe, "Exploring the relative performance of frequency-tracking and fixed-filter phasor measurement unit algorithms under C37.118 test procedures, the effects of interharmonics, and initial attempts at merging P-class response with M-class filtering," *IEEE Trans. Instrum. Meas.*, vol. 62, no. 8, pp. 2140–2153, Aug. 2013.

[9] D. Belega, D. Fontanelli, and D. Petri, "Low-complexity least-squares dynamic synchrophasor estimation based on the discrete Fourier transform," *IEEE Trans. Instrum. Meas.*, vol. 64, no. 12, pp. 3284–3296, Dec. 2015.

[10] V. N. Giotopoulos and G. N. Korres, "A laboratory PMU based on third-order generalized integrator phase-locked loop," *IEEE Trans. Instrum. Meas.*, vol. 73, pp. 1–11, 2024.

[11] C. Huang, X. Xie, and H. Jiang, "Dynamic phasor estimation through DSTKF under transient conditions," *IEEE Trans. Instrum. Meas.*, vol. 66, no. 11, pp. 2929–2936, Nov. 2017.

[12] A. Bashian, D. Macii, D. Fontanelli, and D. Petri, "A tuned whitening-based Taylor-Kalman filter for p class phasor measurement units," *IEEE Trans. Instrum. Meas.*, vol. 71, pp. 1–13, 2022.

[13] J. C. Mayo-Maldonado et al., "Data-driven framework to model identification, event detection, and topology change location using D-PMUs," *IEEE Trans. Instrum. Meas.*, vol. 69, no. 9, pp. 6921–6933, Sep. 2020.

[14] F. Aminifar, F. Rahmatian, and M. Shahidehpour, "State-of-the-art in synchrophasor measurement technology applications in distribution networks and microgrids," *IEEE Access*, vol. 9, pp. 153875–153892, 2021.

[15] V. Ravindran, T. Busatto, S. K. Rönnberg, J. Meyer, and M. H. J. Bollen, "Time-varying interharmonics in different types of grid-tied PV inverter systems," *IEEE Trans. Power Del.*, vol. 35, no. 2, pp. 483–496, Apr. 2020.

[16] P. S. Wright, A. E. Christensen, P. N. Davis, and T. Lippert, "Multiple-site amplitude and phase measurements of harmonics for analysis of harmonic propagation on Bornholm Island," *IEEE Trans. Instrum. Meas.*, vol. 66, no. 6, pp. 1176–1183, Jun. 2017.

[17] J. A. de la O Serna, "Dynamic phasor estimates for power system oscillations," *IEEE Trans. Instrum. Meas.*, vol. 56, no. 5, pp. 1648–1657, Oct. 2007.

[18] M. Bertocco, G. Frigo, C. Narduzzi, C. Muscas, and P. A. Pegoraro, "Compressive sensing of a Taylor-Fourier multifrequency model for synchrophasor estimation," *IEEE Trans. Instrum. Meas.*, vol. 64, no. 12, pp. 3274–3283, Dec. 2015.

[19] S. Toscani, C. Muscas, and P. A. Pegoraro, "Design and performance prediction of space vector-based PMU algorithms," *IEEE Trans. Instrum. Meas.*, vol. 66, no. 3, pp. 394–404, Mar. 2017.

[20] R. Ferrero, P. A. Pegoraro, and S. Toscani, "Proposals and analysis of space vector-based phase-locked-loop techniques for synchrophasor, frequency, and ROCOF measurements," *IEEE Trans. Instrum. Meas.*, vol. 69, no. 5, pp. 2345–2354, May 2020.

[21] F. Messina, P. Marchi, L. Rey Vega, C. G. Galarza, and H. Laiz, "A novel modular positive-sequence synchrophasor estimation algorithm for PMUs," *IEEE Trans. Instrum. Meas.*, vol. 66, no. 6, pp. 1164–1175, Jun. 2017.

[22] P. Castello, R. Ferrero, P. A. Pegoraro, and S. Toscani, "Space vector Taylor-Fourier models for synchrophasor, frequency, and ROCOF measurements in three-phase systems," *IEEE Trans. Instrum. Meas.*, vol. 68, no. 5, pp. 1313–1321, May 2019.

[23] R. Ferrero, P. A. Pegoraro, and S. Toscani, "Synchrophasor estimation for three-phase systems based on Taylor extended Kalman filtering," *IEEE Trans. Instrum. Meas.*, vol. 69, no. 9, pp. 6723–6730, Sep. 2020.

[24] G. Frigo, P. A. Pegoraro, and S. Toscani, "Compressive sensing Taylor-Fourier multifrequency approach for three-phase signals," in *Proc. IEEE 14th Int. Workshop Appl. Meas. Power Syst. (AMPS)*, Sep. 2024, pp. 1–6.

[25] G. Frigo, P. A. Pegoraro, and S. Toscani, "Enhanced support recovery for PMU measurements based on Taylor-Fourier compressive sensing approach," *IEEE Trans. Instrum. Meas.*, vol. 71, pp. 1–11, 2022.

[26] D. L. Donoho and X. Huo, "Uncertainty principles and ideal atomic decomposition," *IEEE Trans. Inf. Theory*, vol. 47, no. 7, pp. 2845–2862, Nov. 2001.

[27] H. Helms, "Digital filters with equiripple or minimax responses," *IEEE Trans. Audio Electroacoustics*, vol. AE-19, no. 1, pp. 87–93, Mar. 1971.

[28] J. Kaiser and R. Schafer, "On the use of the I0-sinh window for spectrum analysis," *IEEE Trans. Acoust., Speech, Signal Process.*, vol. ASSP-28, no. 1, pp. 105–107, Feb. 1980.

[29] P. Castello, R. Ferrero, P. A. Pegoraro, and S. Toscani, "Effect of unbalance on positive-sequence synchrophasor, frequency, and ROCOF estimations," *IEEE Trans. Instrum. Meas.*, vol. 67, no. 5, pp. 1036–1046, May 2018.

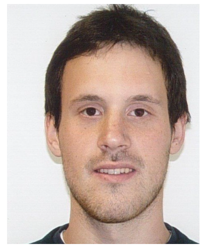

Guglielmo Frigo (Senior Member, IEEE) was born in Padua, Italy, in 1986. He received the B.Sc. and M.Sc. degrees in biomedical engineering from the University of Padova, Padua, in 2008 and 2011, respectively, and the Ph.D. degree from the School of Information Engineering, University of Padova, in 2015, with a dissertation about compressive sensing (CS) theory applications to instrumentation and measurement scenario.

He served as a Post-Doctoral Researcher with the Electronic Measurement Research Group, University of Padova, from 2015 to 2017, and the Distributed Electrical Laboratory, Swiss Federal Institute of Technology, Lausanne, Switzerland, from 2018 to 2020. In 2020, he was a Foreign Guest Researcher with the National Institute of Standards and Technology (NIST), Gaithersburg, MD, USA. He is currently a Scientist at METAS, Bern, Switzerland, where he is responsible for the research strategy in energy and mobility. His current research interests include development of enhanced measurement infrastructures for electrical systems.

Paolo Attilio Pegoraro (Senior Member, IEEE) received the M.S. degree (summa cum laude) in telecommunication engineering and the Ph.D. degree in electronic and telecommunication engineering from the University of Padova, Padua, Italy, in 2001 and 2005, respectively.

From 2015 to 2018, he was an Assistant Professor with the Department of Electrical and Electronic Engineering, University of Cagliari, Cagliari, Italy, where he is currently an Associate Professor. He has authored or co-authored more than 170 scientific papers. His current research interests include design of new measurement techniques for modern power networks, with attention to synchronized measurements and state estimation.

Dr. Pegoraro is a member of IEEE IMS TC 39 (Measurements in Power Systems) and IEC TC 38/WG 47. He is also a member of IEEE EPPC Working Group on Energy. He is the Associate Editor in Chief of IEEE TRANSACTIONS ON INSTRUMENTATION AND MEASUREMENT and the General Chair of the IEEE International Workshop on Applied Measurements for Power Systems (AMPS).

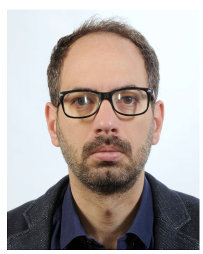

Sergio Toscani (Senior Member, IEEE) received the M.S. and Ph.D. degrees (summa cum laude) in electrical engineering from the Politecnico di Milano, Milan, Italy, in 2007 and 2011, respectively.

From 2011 to 2020, he was an Assistant Professor of Electrical and Electronic Measurement with the Dipartimento di Elettronica, Informazione e Bioingegneria, Politecnico di Milano, where he currently serves as an Associate Professor. His research activity is mainly focused on development and testing of current and voltage transducers, measurement techniques for power systems, electrical components, and systems diagnostics.

Dr. Toscani is member of the IEEE Instrumentation and Measurement Society, the IEEE TC-39—Measurements in Power Systems, and the Technical Program Co-Chair of the IEEE International Workshop on Applied Measurements for Power Systems (AMPS).